ORIGINAL ARTICLE

Analysis of the bond behavior of a GFRP rebar in concrete by in-situ 3D imaging test

Szymon Grzesiak · Tin Barisin · Katja Schladitz · Matthias Pahn[iD]

Abstract Computed tomography combined with mechanical tests offers completely new insight into the behavior of concrete samples under stress. Particularly the development of new fiber reinforcement materials for concrete elements requires appropriate material models and thus for investigating the interior of the concrete structure. In 3D image data obtained by computed tomography, local structural changes within the sample due to mechanical loading can be observed without further altering the sample. We applied this state-of-the-art approach to a concrete core with an embedded glass fiber reinforced polymer rebar under increasing forces applied to pull out the rebar. In this paper, authors describe a novel in-situ setup for non-destructively 3D imaging during the pull-out test. Conducting the pull-out test leads to the formation of local pore volume changes along the rebar. These pore volume changes are not only visualized but quantified analytically based on the images. Interpreting these volume changes, we derive a novel method for calculating strain and normal stresses in the rebar. Our new method captures the detailed distribution of the bond stresses between rebar and concrete and consequently describes the bond behavior more accurate. It turns out that the observed bond behavior cannot be explained completely by commonly assumed material laws. This emphasizes the need for further, more extensive research combining 3D imaging, mechanical testing, and quantitative image analysis.

Keywords Glass fiber reinforced polymer (GFRP) · Reinforced concrete (RC) · Image analysis · Computed tomography (CT)

S. Grzesiak · M. Pahn (✉)
Department of Civil Engineering, University of Kaiserslautern-Landau, Paul-Ehrlich-Straße 14, 67663 Kaiserslautern, Germany
e-mail: matthias.pahn@rptu.de

S. Grzesiak
e-mail: szymon.grzesiak@rptu.de

T. Barisin · K. Schladitz
Image Processing Department, Fraunhofer ITWM, Fraunhofer-Platz 1, 67663 Kaiserslautern, Germany
e-mail: barisin@rptu.de

K. Schladitz
e-mail: katja.schladitz@itwm.fraunhofer.de

1 Introduction

The durability of concrete structures over time is important, in particular the durability of reinforced structures. Over the service life of a building [1], their structure is exposed to different environmental exposure [2]. Therefore, the long-term behavior of construction elements under combined effects of load, moisture, temperature, and environmental exposure should be explored in detail. The commonly used steel

reinforcements suffer from high deadweight and susceptibility to corrosion [3]. Glass fiber reinforced polymer (GFRP) rebars have several advantages over these traditional steel reinforcements like high durability, light weight, and electromagnetic permeability [4–6]. At the same time, GFRP rebars differ from those made of steel in their mechanical properties [7]. The tensile strength of GFRP is at least two times higher than the maximal tensile strength of steel and the modulus of elasticity of GFRP is in the range of one fifth of that of steel [8]. These differences naturally affect the force's transmission from the rebar in the concrete, in particular the bond behavior of the embedded GFRP. It needs also to be mentioned that GFRP has disadvantages, too, due to the characteristics of the material. In addition to the low modulus of elasticity, there are the negative effects of material creep and the limited ductility of GFRP reinforcement. Moreover, this reinforcement type has higher costs compared to mild steel and serviceability problems arising from the low modulus of elasticity. [9].

In general, concrete has good mechanical compressive properties. The material is a combination of aggregates, cement and water. During its production, pores and micro pores are formed in the structure. One of the disadvantages of concrete is its low tensile strength. Cracks form easily under tension and the material can resist almost no tensile forces. The positive effect of reinforcements in concrete members has been known for more than 70 years [10]. Steel rebars in concrete absorb tensile forces that the concrete cannot withstand due to its low tensile strength. The tensile forces in the reinforced concrete components are transmitted via a bond between rebar and concrete. The arising shear bond stresses have three components: adhesive, frictional, and interlocking mechanisms [11, 12]. Parameters such as rebar diameter or contact surface area influence the transmission of forces and the anchorage length of the rebar. All these parameters affect the capacity of the structure in the ultimate limit state (ULS) and the serviceability limit state (SLS) design analyses [13, 14]. The anchorage length of the rebar in concrete is the minimal embedment length of reinforcement to transfer the bond forces and therefore tension forces.

The Anchorage length of concreting rebars is associated with stress distribution between reinforcement and concrete matrix. Describing stresses and strains along the rebar in the concrete member detailed and precisely reflects the general behaviour of the transfer of forces in the interior of reinforced elements and becomes increasingly important. The common assumption of constant or averaged bond stresses for FRP rebars in concrete is a simplification [15, 16]. There are some bond behavior models, which describe a non-uniform distribution of stresses. They were developed based on empirical or numerical data [17–21] and for specific types of reinforcement. For the experimental validation of these models, the shear stresses along the rebar should be carefully investigated, to indicate the bond behavior law. It is of particular interest to calibrate the existing models for the local bond strength like the Bertero-Popov-Eligehausen (BPE) [22, 23] or the modified Bertero-Popov-Eligehausen (mBPE) models [24].

Current measurement methods for the bond behavior of rebars embedded in concrete are based on the strain-slip relationship [25]. A displacement transducer measures the slip between concrete surface and rebar, while the concreted rebar is pulled out with a constant force [26]. Strain gauges are attached to the GFRP bar at the middle of the sample [27]. In the literature, three different test setups for GFRP reinforced concrete samples with a partially (with bond length 5 Ø), a short-bonded (with bond length equal the rib lead + 1 mm), and a fully bonded area are well known. The shear bond-slip law can be applied under the assumption of constant bond stresses as fulfilled in the case of a short embedment length [28, 29]. Unfortunately, for higher contact lengths, the stress-slip relation has to be adjusted more precisely to describe the non-uniform mechanical properties of the bond [30]. For the concrete sample with fully bonded area, the bond stress at the beginning differs from the one at the end of the embedded rebar. The slip is measured only at the end of the GFRP rebar, in spite of the slip being not constant and increasing faster at the beginning of the bonded area [31]. Due to this incremental deformation, common test setups cannot reconstruct the bond stress curves along the rebar realistically and thus do not yield a proper bond-slip constitutive law.

The problem of the varying bond stresses along the rebar could be solved by quasi-continuous measurement [32]. Computed tomography (CT) yields the perfect solution [33] as it enables non-destructive observation of the inner structure of materials [34]. Moreover, CT allows to analyze a whole concrete

specimen [35] and thus opens new opportunities for investigating and comparing a variety of concrete types and mechanical properties i.e. porosity, density or damage and failure [36]. Furthermore, the increase of cracks between embedded rebar and concrete can be tracked in the sample after performing the pull-out test [37, 38], fiber positions in fiber reinforced concrete samples can be determined [39], or corrosion effects and formation of pores near a steel rebar can be studied [40, 41].

The aim of this paper is to develop a methodology for estimating the bond behavior between GFRP and concrete from 3D CT image data. To the best of our knowledge, this has not been reported previously.

The GFRP rebar was embedded in concrete and subjected to three tensile loading stages. The concrete sample including the rebar was CT scanned while the tensile force had been applied. The resulting three reconstructed 3D images were processed to identify the rebar, the concrete, and pores in the sample. Subsequently, the pore growth induced by the applied pull-out force could be quantified. The observed local pore volume changes can be attributed to stress and strains in the GFRP that are transferred to the concrete cover. Finally, from the pore volume changes, bond stresses were derived, analyzed, and compared with theoretical models from the literature. One of the bond-slip constitutive laws was found to agree well with the experimental results and to fit the observed distribution of bond stresses along the GFRP reinforcement, as well as the anchorage length of the rebar in concrete.

The novelty of this paper is two-fold. First, the in-situ CT imaging and pull-out testing for the GFRP rebar enforced concrete sample is described for the first time. Second, we develop a methodology for quantifying the effects of this pull-out test in terms of strain and bond stresses. Our study thus contributes to the development of GFRP reinforcements as an alternative to traditional steel reinforcements.

2 Experimental investigation

2.1 Experimental program

The bond behavior of the concreted GFRP rebar was examined through a pull-out test as shown in Fig. 1. The GFRP rebar is concreted in a cylindrical formwork. Loading was applied by a hydraulic actuator and measured using a load cell. The GFRP rebar was fixed by a threaded steel tube and cement mortar filling. A joint bearing distributed the force symmetrically. To prevent formation of a concrete cone, the first 20 mm of the concreted rebar were coated with an adhesive tape (located on the Z-axis between -5.0 and -3.0 cm). This part of the GFRP rebar was not bonded to the concrete and was loaded with the maximal force introduced by the hydraulic cylinder (see 8 in Fig. 1). Finally, the region between 0.0 and 14.4 cm on the z-axis was scanned.

The concrete sample's inner structure changes during loading. Therefore, during each pull-out test phase (unloaded or with constant loads 18 kN, 25 kN, see Table 1), the concrete was scanned and its inner structure was analyzed with a special focus on changes due to the applied load. The load stages 18 kN and 25 kN correspond to 25% and 34% of the tensile strength of the GFRP rebar $f_{t,m}$, respectively. The ratio η of the rebar stress σ_{GFRP} to tensile strength is determined by Eq. 1.

$$\eta = \frac{\sigma_{\text{GFRP}}}{f_{t,m}} \tag{1}$$

2.2 Materials

The concrete formulation is summarized in Table 2. In the experiment, sand and gravel from the Rhein region were used in the mix. The maximum aggregate size was 8 mm [42] to enable a good distribution of the concrete mixture in the narrow formwork. Cement CEM II 32.5 and water were used in w/c ratio 0.70. The purpose of such a high w/c ratio was to achieve the highest possible porosity in normal concrete. Chen et al. [43] showed that the pore size distribution in cement paste depends on the amount of water and cement. They tested various ratios starting at 0.3 and found the highest porosity for the ratio of 0.7. The sample was prepared and stored indoor at room temperature (20 ± 2 °C) and a relative humidity ($65 \pm 5\%$) [44]. At the age of 28 days, concrete specimens were tested for compressive strength [45], which was 26.34 MPa.

Typical fibers for FRP rebars are made of glass [46]. They are quite common in industrial and engineering applications. In this study, the rebar was
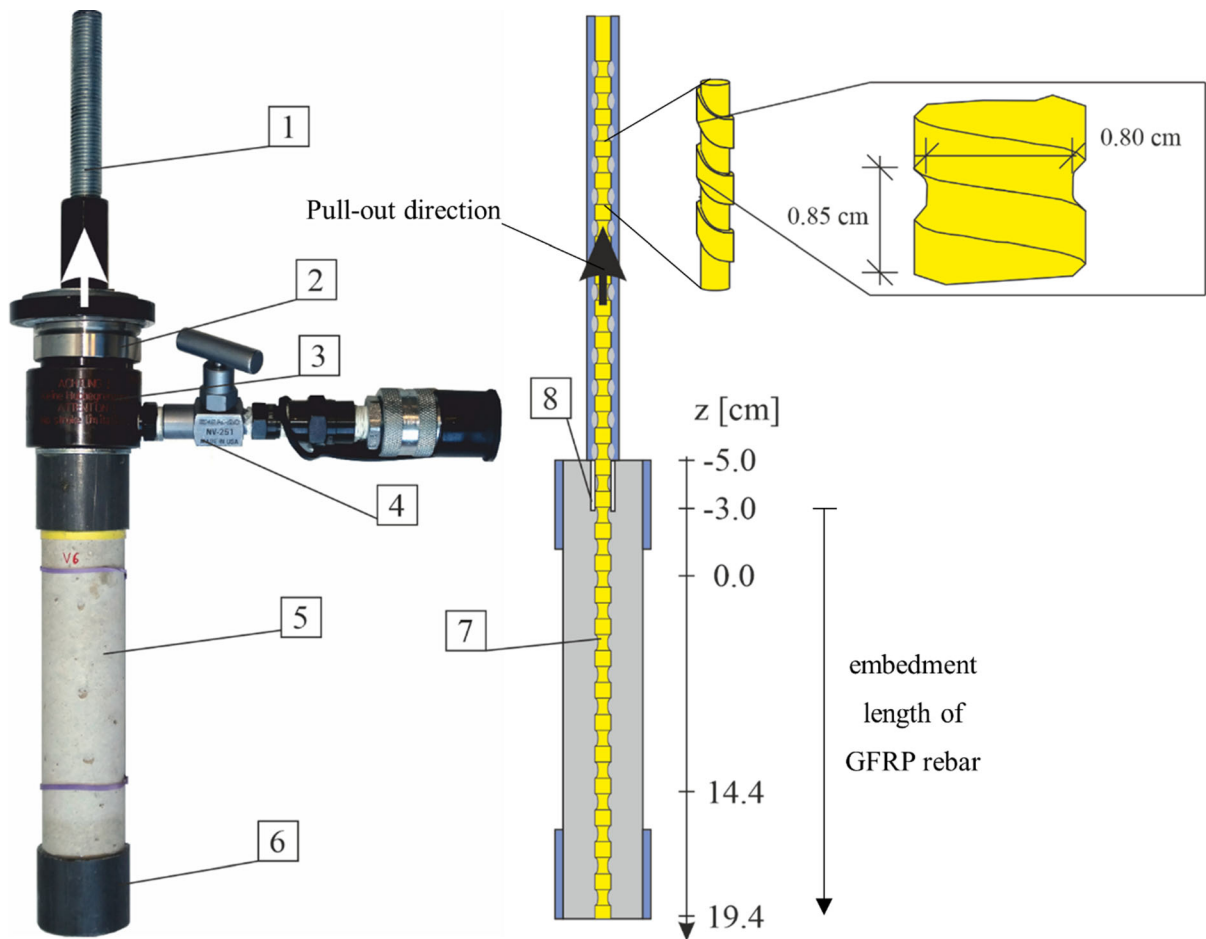
Fig. 1 Experimental setup: 1—Steel fixing of GFRP rebar with cement mortar filling, 2—Joint bearing, 3—Hydraulic cylinder, 4—Hydraulic system, 5—Concrete sample, 6—CT sample adjustment, 7—GFRP rebar, 8—Adhesive tape for non-bonded area

Table 1 Overview of experimental program:

No	Load F_{GFRP}	Strain in GFRP rebar ε_{GFRP}	Stress in GFRP rebar σ_{GFRP}	Load factor η of tensile strength
	(kN)	(‰)	(MPa)	(%)
1	unloaded	0	0	0
2	18	5.52	358	25
3	25	7.66	497	34

reinforced by endless glass fibers with a diameter of approximately 20 μm [47] produced in the form of rovings. During the pultrusion process, the glass fibers were impregnated with a vinyl ester resin to improve the bonding of the fibers and the matrix and to protect fibers against mechanical, chemical, and physical damage [5]. The fiber content of the GFRP rebar was approximately 65 wt% and the GFRP density was 2.2 kg/mm³.

Finally, rebars were cut, coated, and ribs were cut on the surface. The final GFRP rebar had a trapezoidal threaded profile and an outer diameter Ø of 8.0 mm [48]. The ribbed surface of the rebar helically

surrounded the core of the rod. It was covered by $c = 15$ mm of concrete throughout the sample.

The characteristics of the GFRP rebar were tested according to [49]. The value of tensile strength, elastic modulus and maximum fracture strain are summarized in Table 3. The high strength of the glass fibers is passed on to the strength of the FRP product in axial direction.

2.3 In-situ CT measurements

CT enables unique, non-destructive insight into 3D microstructures [50]. From classical X-ray absorption projection images taken at many angles, a 3D image is computed that recovers the full spatial structural information [51, 52]. The most important components of a typical laboratory CT device are the X-ray emitting tube, the turntable holding the sample, and the flat-bed detector. During the scan, the sample is rotated by a predefined angular increment. In each position, a 2D X-ray projection image is taken. Finally, the 3D image of the sample is reconstructed computationally from the projections.

In laboratory CT devices, the X-rays usually form a cone. The position of the sample between X-ray tube and detector therefore controls the magnification and together with number and size of the detector pixels the voxel size in the reconstructed 3D image. The voxel gray values represent essentially local X-ray attenuation, which in turn depends on the atomic numbers of the elements passed by the beam. Concrete matrix, GFRP reinforcement, and air filled pores absorb X-rays differently. Thus, the corresponding voxels should feature different gray values, too. The heterogeneous composition and varying density of the concrete however result in varying voxel gray values within the concrete matrix. Visually, higher gray values express themselves as brighter appearance of the voxels. In Fig. 3, the difference between X-ray absorption properties of concrete components is shown: cement paste (intermediate, gray), air pores (low, dark), and aggregates (strong, bright).

The sample was scanned using the CT device at Fraunhofer ITWM (Kaiserslautern, Germany) featuring a Feinfocus FXE 225.51 X-ray tube with maximum acceleration voltage 180.3 kV, maximum power 12.7 W, and a Perkin Elmer flat-bed detector XRD 1621 with $2\,048 \times 2\,048$ pixels (Fig. 2a). Here, a tube voltage of 180 kV and an integration time of 5 s were chosen. Tomographic reconstructions were obtained from 800 projections, each averaged over four, resulting in an overall integration time of 20 s. The voxel edge length was around 80 μm, see Table 4. Figure 2b shows the test setup with the concrete sample mounted for the unloaded sample and Fig. 2c for stages 18 kN and 25 kN.

3 Analytical and experimental investigation

3.1 Image processing

CT scanning yielded a 3D image of the concrete microstructure in each of the three stages of the pull-out test. The voxels had gray values in the 16 bit integer range. Original image sizes are given in Table 4. The negative z-direction of the images corresponds to the loading direction during the pull-out test (as shown in Fig. 1). Images were processed and analyzed using the software tools MAVI and ToolIP [53, 54].

Table 2 Concrete mix design:

Material	Raw density ρ (kg/m^3)	Weight m (kg/m^3)
Cement (CEM II 32,5)	3100	280
Aggregate 0 to 2 mm	2600	740
Aggregate 2 to 8 mm	2600	900
Water	1000	195

Table 3 Mechanical properties of the GFRP (average value over five tests) [49]:

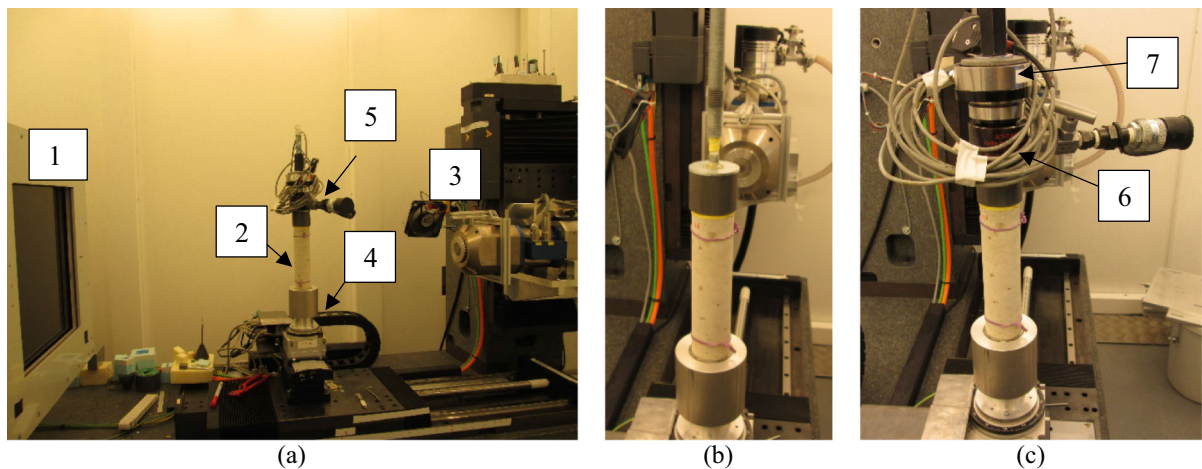| Material	Diameter ϕ (mm)	Fracture strain $\varepsilon_{u,m}$ (%)	E-Modul E_m (GPa)	Tensile strength $f_{t,m}$ (MPa)
GFRP	8.0	2.59 (0.02)	66,618 (682)	1,453 (4)

Fig. 2 **a** Experimental setup with: 1—flat-bed detector, 2—concrete specimen, 3—X-ray source, 4—turntable, 5—system for pull-out experiment, **b** CT imaging of the unloaded concrete sample without hydraulic system, **c** CT imaging of the concrete sample in load stages 18 and 25 kN: 6—hydraulic system and 7—load cell

Table 4 Summary of results after segmentation of pore volume change:

	Slice area (mm^2)	Pore volume change (mm^3)	Voxel size (µm)	Original image size
Unloaded	118.10	75.86	80.50	$1049 \times 1049 \times 1850$
18 kN	117.72	83.75	80.37	$1161 \times 1161 \times 1832$
25 kN	117.09	96.27	80.15	$895 \times 895 \times 1886$

In the reconstructed CT images, several components of the material could be observed: the rebar (gray in the center), air pores (dark), aggregates (bright), and cement paste (gray), see Fig. 3. Image processing aimed at distinguishing these components in the image and analyzing them subsequently. Identification and separation of components or objects in an image is called segmentation. In medical applications, this is often achieved by expert interaction. For the concrete components in the CT images, this approach was not feasible for several reasons. First, the scans were large (order of 2000^3 voxels). Second, the matrix was heterogeneous, gray values therefore varied strongly in very small regions. Hence, interactive segmentation of the concrete components would have been time-consuming and error-prone. Therefore, objective image segmentation methods had to be designed and applied. Special care was taken to ensure that images scanned at different time steps remained comparable at each processing step [27].

As a first step, the area close to the rebar was extracted for each image. Images were cropped to $250 \times 250 \times 1\,800$ voxels (as illustrated in Fig. 3, Step 1 → 2) to investigate this part of the CT images more easily. No changes in the microstructure could be visually identified outside of this area of the interest. Consequently, the remaining/surrounding parts of images were discarded and not used for the analysis. Changes in the extracted area of interest were observed as creation and growth of dark pores on the interface between concrete and rebar (Fig. 4 and Fig. 5).

We aimed at segmenting those structures. However, pores occurring "naturally" in the concrete had the same gray value as those occurring due to damage around the rebar as both were air filled. The former were, however, spherically shaped. Figure 4 shows 2D xy-slices collected from several points in z-direction: voxel 20 (0.4 cm), 300 (2.4 cm), 500 (4.0 cm), and 720 (5.8 cm), respectively. Figure 5 shows xy-slice views where theses z-positions are marked by white lines.

The pore volume V_{pore} around the rebar decreased with growing z-coordinate already for the unloaded sample due to better compaction of the lower part of the concrete in the sample. At higher load states, the
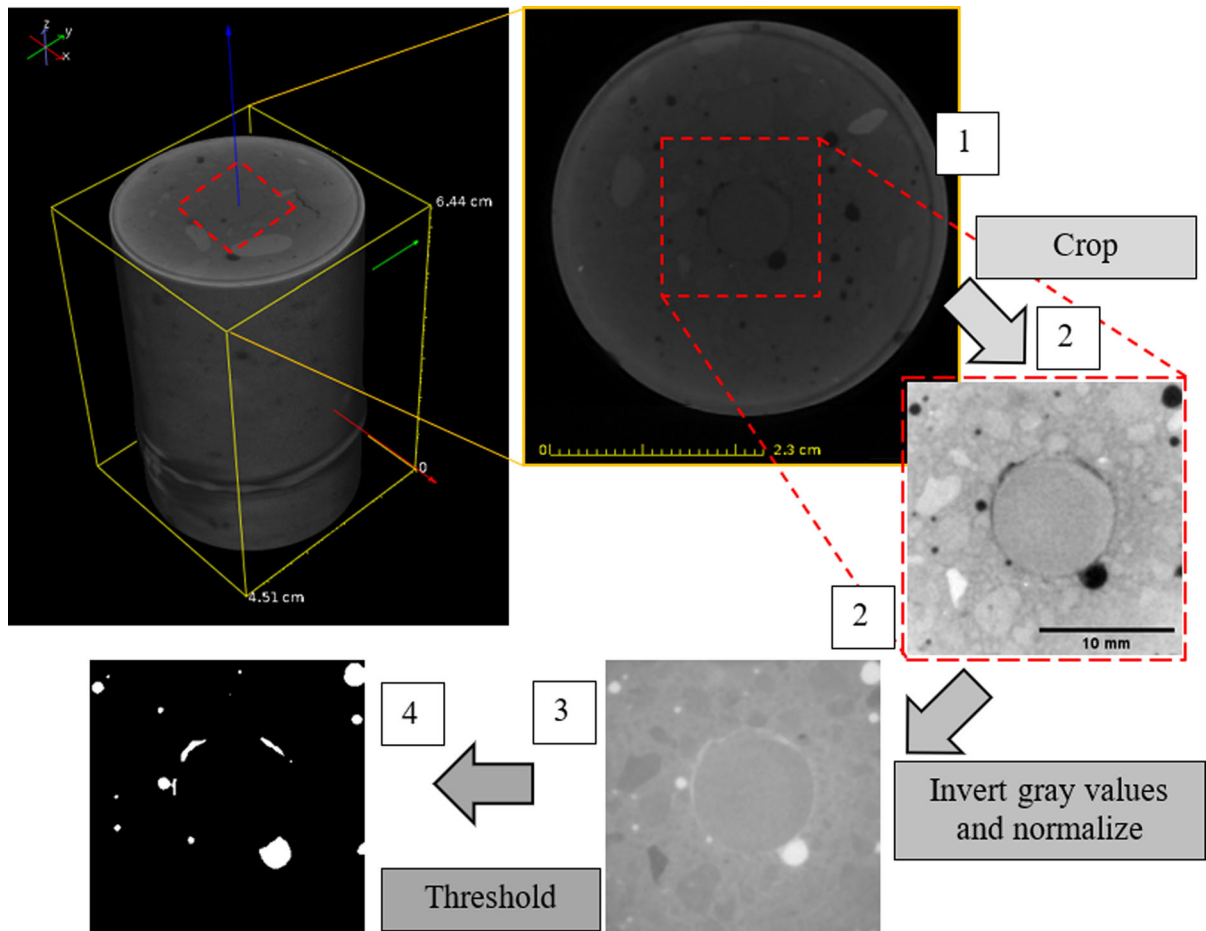
Fig. 3 Reconstructed CT images: 2D slice from the 3D image. The region close to the bar is marked by a red square. The original image size is 1 049 × 1 049 × 1 850 voxels of edge length 80.5 μm cropped to the image size of 560 × 560 × 800 voxels for visualization. The rendering contains the first 800 slices in z-direction from the top in z-direction. Thus 6.44 cm of the sample are shown. Step-by-step image analysis pipeline applied to the 3D images, visualized using a 2D slice parallel to the xy-plane. Step 1—input, initial CT image (zone of interest marked by the red square), step 2—crop the zone of interest, step 3—preprocessing: invert the gray values and mean-std normalize them, step 4—apply a global gray value threshold. Result: segmented volume changes around the rebar and air pores in the zone of interest

pore volume decreased more over the height in the direction opposite to the loading direction. See Fig. 1. The pore volume change ΔV_{pore} from one stage to the other of the pull-out test decreased with growing z-coordinate (Fig. 4). The deformation of the GFRP rebar profile induced growth of the pores originally created during concreting. For example, at slice 700 (5.8 cm), the pores did nearly not grow during all three stages, whereas at slice 20 (0.4 cm), the pore growth is clearly visible (Fig. 4).

Although having been taken consecutively and using constant CT scan parameters, the three images differed slightly in gray value distribution. To ensure comparability, we therefore preprocessed and normalize them as sketched in Fig. 3:

1. Invert the input image gray values (since structures of interest were dark) as shown in Fig. 3, Step 2 → 3,
2. Normalize the gray values by voxel wise subtraction and division to yield mean 0 and variance 1. After the previous two steps, gray value distributions in all three images were in the same range. Hence, the global gray value threshold $t = 2$ then yielded the damage/pore voxels in the area of interest (as shown in Fig. 3, Step 3 → 4). That is, we got so-called binary images where each voxel
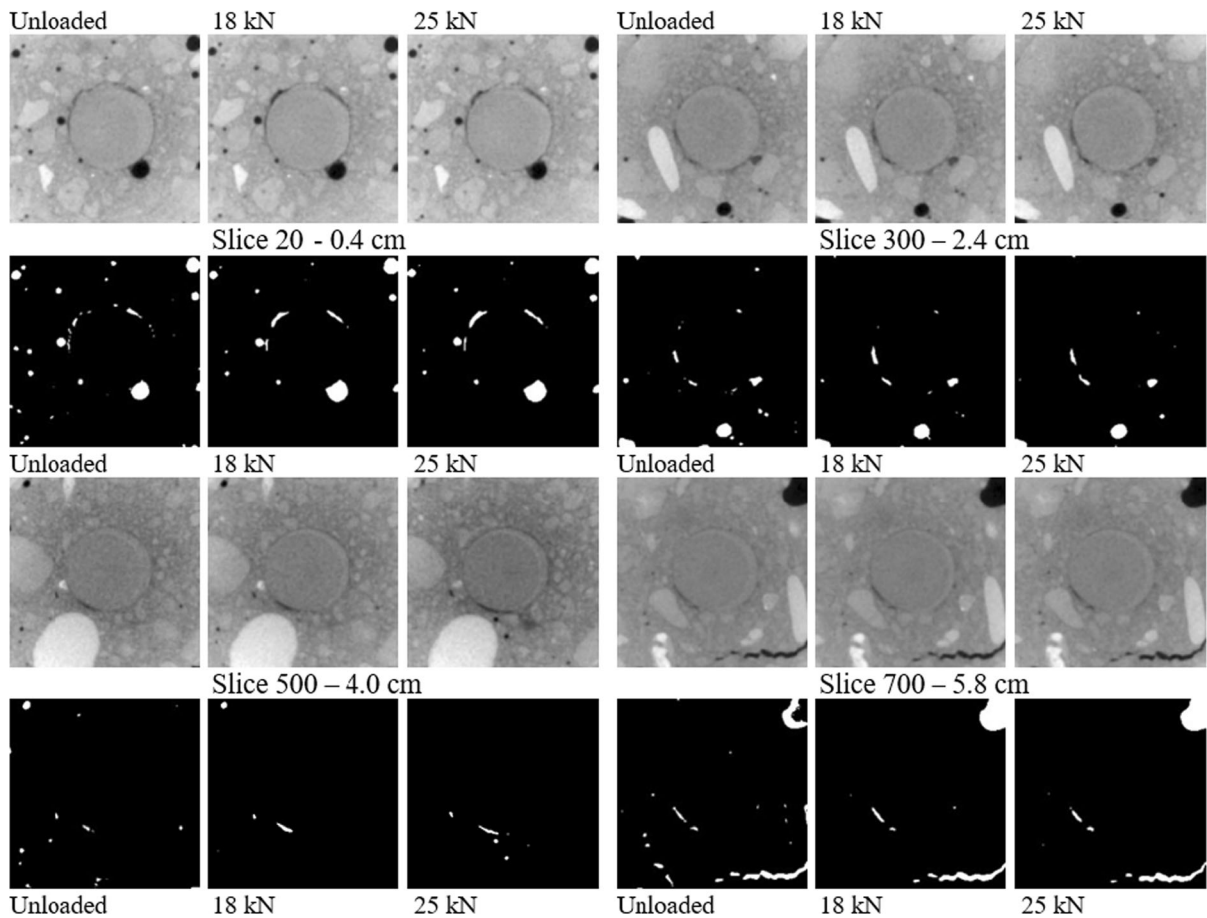
Fig. 4 Sample comparison: xy-slice views (250 × 250 pixels) of the concrete sample at the three stages of the pull-out test (first row) and segmented damaged regions and pores (second row). For voxel sizes see Table 4

can attain value 0 or 1, only. Here, 0 s represent concrete or rebar (gray value lower than t). On the other hand, 1 s represent pores or damage in the sample (gray value higher than t). See Fig. 6 for 2D xy-slices (0 s → black, 1 s → white) and Fig. 9 for volume renderings of the resulting pore systems.

Large spherical pores inside of the concrete matrix did not grow visually conceivably due to the tensile load applied. In order to detect small changes in the pore system, the original pores were removed using a morphological opening [55] with a cubic structuring element of edge length 3.

Results are rendered in Fig. 6. The damaged regions grew with increase of the pull-out force and their shapes changed. These changes followed the spiral profile of the rebar. Figure 6 shows the local

pore volume change around the rebar in the three stages as a function of height (z-coordinate) with a step width of 2 mm. The step width of 2 mm exceeds the voxel length. Thus, the reported volume changes were summed values over several xy-slices in order to alleviate the slight difference in voxel edge lengths in the three CT images (Table 4). Due to this variation, slices in different loading states could not be perfectly matched and slice wise calculation would have resulted in noisy pore volume changes. To reduce this effect, pore volumes were calculated as the sum of volumes from several slices at the bigger sampling step of 2 mm.

Clearly, the concreting process had an impact on the distribution of pores in the sample. The GFRP rebar was attached to the center of the cylindrical formwork in vertical position. The sample was concreted in the mold from one side. From the
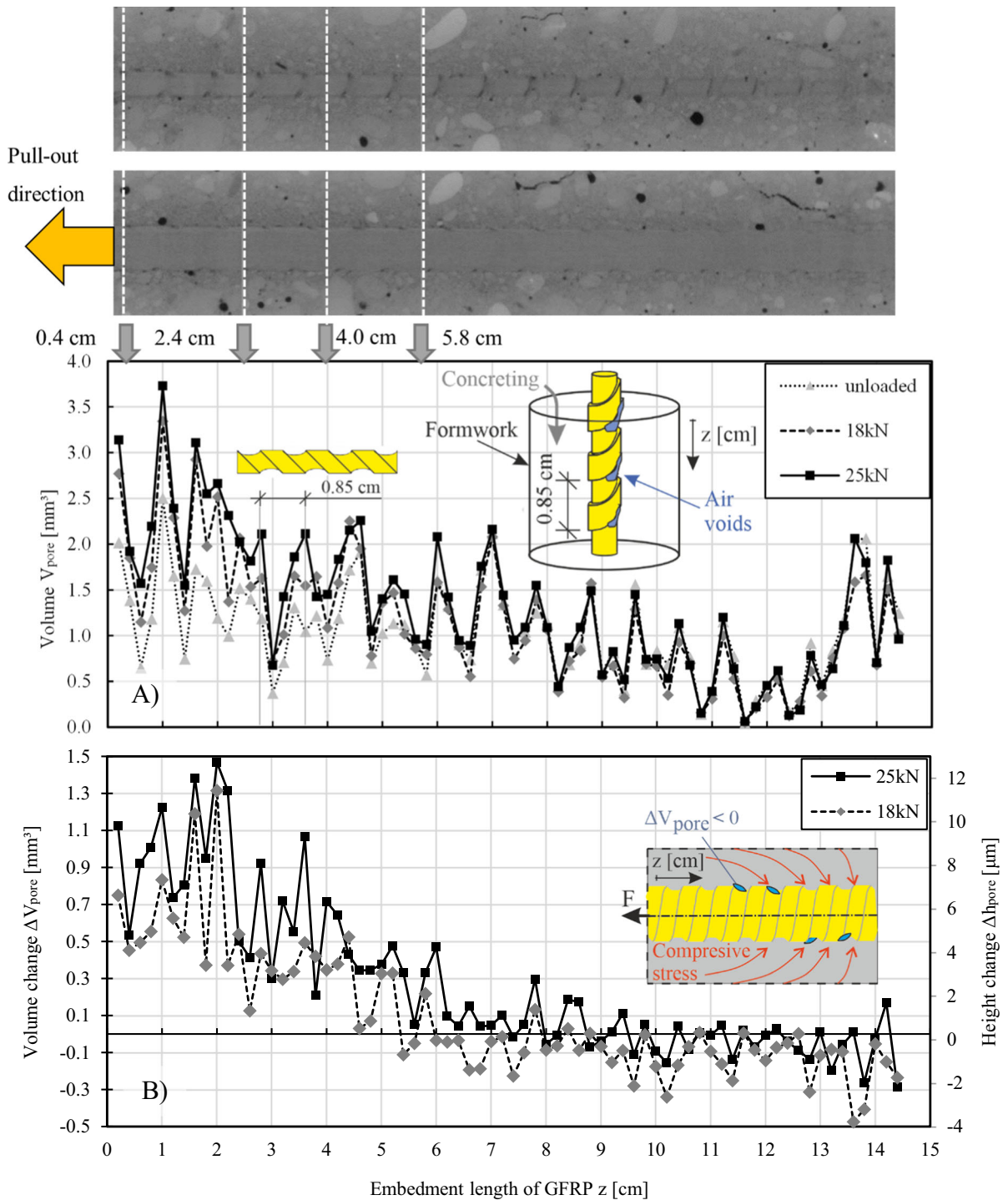
Fig. 5 2D xz-slice views through the CT image at 18 kN loading. The image size is 1 800 × 250 voxels corresponding to 14.4 cm. The xy-slices at heights 20 (0.4 cm), 300 (2.4 cm), 500 (4.0 cm), and 700 (5.8 cm) voxels marked by arrows are those featured in Fig. 4. **a** Pore volume in the test specimen, **b** Changes of local pore volume in the test specimen (2 mm slice sampling)
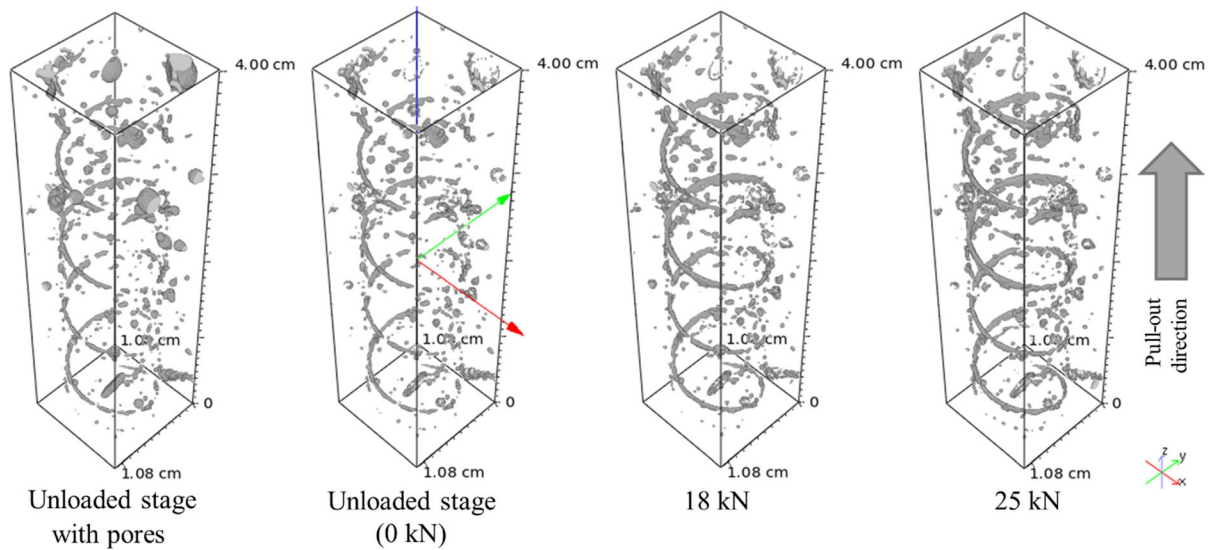
Fig. 6 3D renderings of the first 500 slices from the top of the reconstructed CT images in each phase of the pull-out test. The pore system was rendered while rebar and concrete matrix were completely transparent here. The images were cut to 250 × 250 × 500 voxels of approximate edge length 80 μm (exact values in Table 4) corresponding to 20 mm × 20 mm × 40 mm

opposite side, the surface adhesion of the rebar pushed the liquid concrete away to form a convex meniscus. Subsequently, the air bubbles form on one side below the trapezoidal spiral profile of the GFRP. The rebar had a circular cross-section, diameter 8 mm, and a profile with rib lead 8.5 mm [48]. The local pore volume change in 4 mm thick slices, as depicted in Fig. 6, featured peak concentrations of pores at exactly the distance corresponding to this width of 8.5 mm of the trapezoidal spiral profile on the rebar.

$$\Delta V_{\text{pore}} = V_{\text{loaded stage}} - V_{\text{reference}} \quad (2)$$

From the total local pore volume shown in Fig. 6, the corresponding volume changes $\Delta V_{18kN} = V_{18kN} - V_{0kN}$ and $\Delta V_{25kN} = V_{25kN} - V_{0kN}$ could be deduced (Eq. 2). The most significant volume changes were observed at the side of force application (at the beginning of the z-axis). Volume changes at the end of the z-axis were negative ($\Delta V_{pore} < 0$) due to pores in the concrete being closed. This was observed only on the bottom of the sample and could be explained by lateral compressive stresses in the concrete in this part of the sample (Fig. 5). Furthermore, the height in the sample where the volume changes turned from positive to negative, illustrated the effective anchorage length of the GFRP rebar (between 5 and 8 cm on the z-axis).

3.2 Stress–strain distribution

The experiment revealed, that the pore volume changes ΔV_{pore} accumulated at the beginning of the GFRP rebar (see Fig. 6). This can be attributed to material properties and stiffness of the GFRP bar [56]. The circular concrete cross-section A_{slice} and slice volume V_{slice} were constant for each load step: $A_{\text{slice}} = $ const and $V_{\text{slice}} = $ const, as the same slices were imaged and analyzed. Based on this assumption, we deduced that the air voids were compressed in z-direction in the loaded concrete sample. Therefore, it can be argued that for a unidirectionally loaded sample, the pore volume changes ΔV_{pore} are proportional to the height changes Δh_{pore} of air void in the sample. The pore volume changes can be discretized as $\Delta V_{\text{pore}} = A_{\text{slice}} \cdot \Delta h_{\text{pore}}$. The sketch in Fig. 7 illustrates the pore volume change in the concrete that had been observed during the test. The volume changes accumulated on the side where the force was applied. Further down in the sample, along the Z-axis, the volume change decreased. This is particularly visible near the GFRP rebar. More precisely, the most significant changes are visible near the surface profile of bar. The helically ribbed surface affected the concrete surface area in contact with the rebar and finally influenced the bond behavior [57].
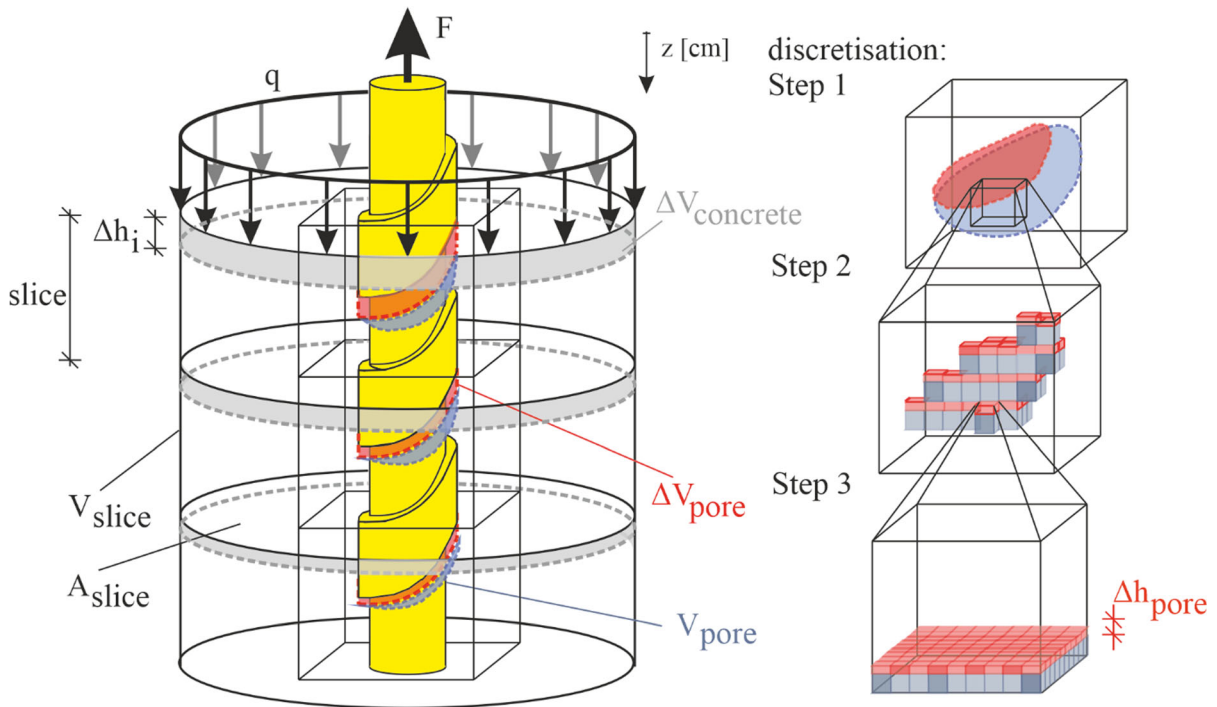
Fig. 7 Expected volume change ΔV_{pore} in the concrete during the test

At higher load steps, the strain in the GFRP rebar increased. The reinforcement deformed and moved from the initial position (unloaded stage) to the deformed position under load. Compared to the unloaded condition, strain and stresses increased in the GFRP as well as in the concrete. The observed bond stress relationship is nonlinear, as explained in the foreword. It may roughly be assumed that the change of volume height Δh_{pore} along the axis of the rebar is equal to the slip s between concrete and GFRP rebar including load and initial state (Eq. 3).

$$s(F_{GFRP}, z) = h_{pore}(F_{GFRP}, z) - h_{pore}(0, z) \qquad (3)$$

The pore volume change equals the deformation of the reinforcement, which in turn equals the strain in the reinforcement bar $\Delta\varepsilon$, i.e. $\Delta\varepsilon = \Delta l/l$ with length l of the bar, or after discretization $\Delta\varepsilon = \Delta h/h$ with Δh denoting the height changes of pores in the sample. The smaller the height steps from slice to slice, the more accurate the determination of the strain [53]. It is significant that due to uniaxial loading these changes are observed in one direction. Therefore, the changes are discretized (step 1 to 3 in Fig. 7) in the direction of the GFRP rebar axis (z-direction). Figure 8 presents

the strain curve for load steps 18 kN and 25 kN. The strain values ε in the region higher up (height -3.0 to 0 cm) and thus not captured by the CT scans were calculated based on Hook's law $\varepsilon_{GFRP} = \sigma_{GFRP}/E_m$ [54] where E_m and σ_{GFRP} are Young's modulus and stress of the GFRP rebar, respectively. Stress could be derived from the equation $\sigma_{GFRP} = F_{GFRP}/A_{GFRP}$, assuming a circular cross-section ignoring the trapezoidal threaded profile.

4 Results and discussion

4.1 Stress–strain relationship

The rebar's maximal stress under the two different load steps were 358 and 497 MPa, respectively. The stresses in the scanned region (between 0.0 and 14.4 cm in z-direction) were calculated based on Hook's law with known strain ε (Fig. 8). In the region at the top of the sample (height -3.0 to 0.0 cm), that was not imaged, a course of the stress and the corresponding strains in the GFRP bar could nevertheless be extrapolated as shown in Fig. 9 by dashed lines for 18 kN and 25 kN.
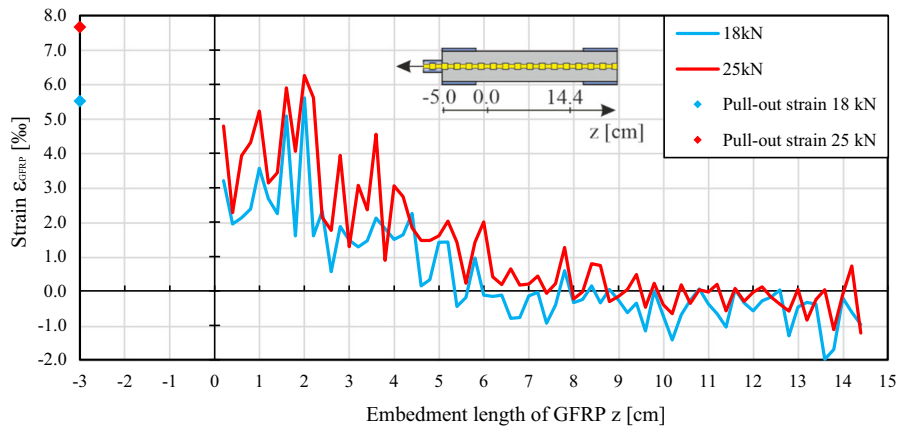
Fig. 8 Strain curve for load steps 18 kN and 25 kN (2 mm slices)
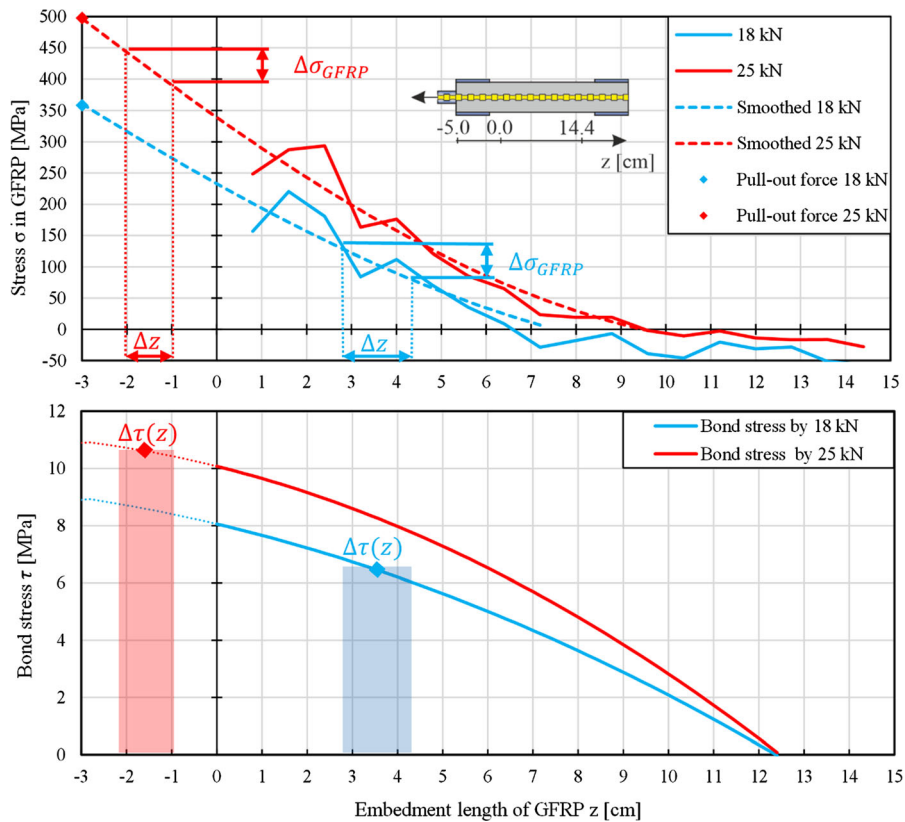

Fig. 9 Stress curves and smoothed bond stress curves for load steps 18 kN and 25 kN (8 mm slices)

Predictions and experimental results for stresses in the scanned region and stress in the rebar on the point of pull-out force correspond well. This can be emphasized by connecting the point of maximal stress with the stress curve in the scanned region by a smoothed trend line.

The concrete strains were calculated based on Young's modulus for concrete according to DIN 12390–13 [59]. The largest concrete deformations were concentrated near the sample's face directed towards the axial force. Along the height of the sample, the force in the rebar and the

corresponding strain decreased. In the following sections, the bond stress τ is defined [20] as the correlation between normal stress σ_{GFRP} deduced from the smoothed trend line based on measurement data and the rebar geometry (Eq. 4).

$$\tau(z) = \frac{A_{\text{GFRP}} \cdot \Delta\sigma_{\text{GFRP}}(z)}{h_{\text{slice}} \cdot 2\pi r} \tag{4}$$

The bond stress along the Z-axis is presented in Fig. 9.

4.2 Analytical model of the bond-slip behavior

The strains in the GFRP rebar are concentrated at the beginning of the bond area in the sample. The overall behavior suggests that the region with the highest normal stresses could have already debonded albeit only partially, where the adhesion forces had been exceeded. The trapezoidally threaded profile blocks larger displacements. In a further section of the rebar, the bond stress does not reach its maximum. According to [60] the peak value of bond strength in splitting failure mode depends on the rebar diameter, bond conditions (rebar profile), concrete strength, and thickness of the concrete cover. No perpendicular splitting cracks were observed in the experiment. This indicates that the 15 mm concrete cover is nevertheless sufficiently thick.

As a further step in the analysis, bond stresses were compared with theoretical models from the literature. For these models, local bond stress over the rebar length in the pull-out test can be determined by stepwise integration of the strain and stress in discretized z-direction for small sections $\Delta z = z_{i-1} - z_i$ by an iterative four step procedure [18, 20]. Here, z_{i-1} is the beginning and z_i is the end of the small z-axis interval sampled. The boundary conditions are a known initial slip value s_i and zero normal stress at the end of the rebar. At the beginning, an exponential function $\tau(s)$ is used to describe the bond-slip constitutive law [19] (Eq. 5).

$$\tau(s) = C \cdot s^{\alpha}(z), \tag{5}$$

where coefficients α and C describe the ascending branch of the curve for s_{i-1} (Eq. 6) [18, 57].

$$\tau_{i-1}(s_{i-1}) = C \cdot (s_{i-1})^{\alpha} \tag{6}$$

$$\sigma_i = \sigma_{i-1} + \tau_{i-1} \cdot \Delta z \cdot \frac{2\pi r}{A_{\text{GFRP}}} \tag{7}$$

$$\varepsilon_i = \frac{\sigma_{i-1}}{E_m} \tag{8}$$

$$s_i = \frac{\varepsilon_i + \varepsilon_{i-1}}{2} \cdot \Delta z + s_{i-1} \tag{9}$$

Second, the bond stresses τ are converted to axial stresses σ in the GFRP rebar (Eq. 7). Based on Hook's law, the strains ε are computed (Eq. 8). Finally, the relative displacement s_{i-1} is increased by the Δs value to obtain s_i (Eq. 9).

These iteration steps were repeated eighty times, which corresponded to a proper discretization of the rebar length as suggested by Małecki [61]. Furthermore, the length of the element Δz agreed with the slice thickness of 2 mm selected for image processing. The final computed force was compared with the force measured during the pull-out test. Moreover, the bond stress diagram along the length of the GFRP rebar was derived. The location on the z-axis, where the GFRP-rebar is no more loaded, shows the anchorage length of reinforcement in concrete.

The parameters of the bond-slip for the applied constitutive law are presented in Table 5. The softening branch was not analyzed because the slip calculated from the experimental tests did not exceed the end slip of $s_1 = 0.75$ mm. Therefore, the tests were recalculated based on the ascending branch, only.

In [19], empirical coefficients C, also known as average bond strength τ_{max}, and exponent α are proposed for the same GFRP rebar (Table 3). Niewels [62], Pecce et al. [17], and Cosenza et al. [17, 63] derived the bond law with coefficients C and α experimentally. Figure 10 compares the bond-slip law to the bond stress-slip relation derived from our in-situ test. Our bond stress values differ from those obtained in the previous experiments. These differences can be explained by the concrete samples examined: Niewels [62] used a concrete with compressive strength 34.2 MPa for the tests with a similar GFRP rebar of diameter 8 mm. Pecce and Cosenza calibrated their model on a sample with a compressive concrete strength ranging between 39 and 52 MPa. Thus, our concrete sample's compressive strength of 26.34 MPa is considerably lower than those of the previously investigated ones. As a consequence, the observed deviation is not surprising as local bond stresses are

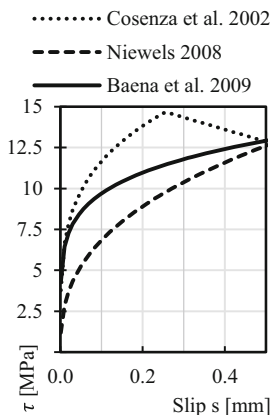**Table 5** Bond coefficients C and α for the tested pull-out specimen [17–21, 62, 63]

	Pecce et al. 2001 Cosenza et al. 2002	Niewels 2008	Baena et al. 2009	
C	20.5	16.41	17.3	⋯⋯⋯ Cosenza et al. 2002
A	0.25	0.38	0.18	– – – Niewels 2008
s_1	0.25	0.75	$s_m = 2.619$	—— Baena et al. 2009
$\tau(s)$ for $s > s_1$	$\tau(s) = 14.6 - 7.4 \cdot s$	–	–	

Fig. 10 Comparison of the bond law and the bond stress-slip relation derived from the in-situ pull-out tests with GFRP rebar for load steps **a** 18 kN and **b** 25 kN
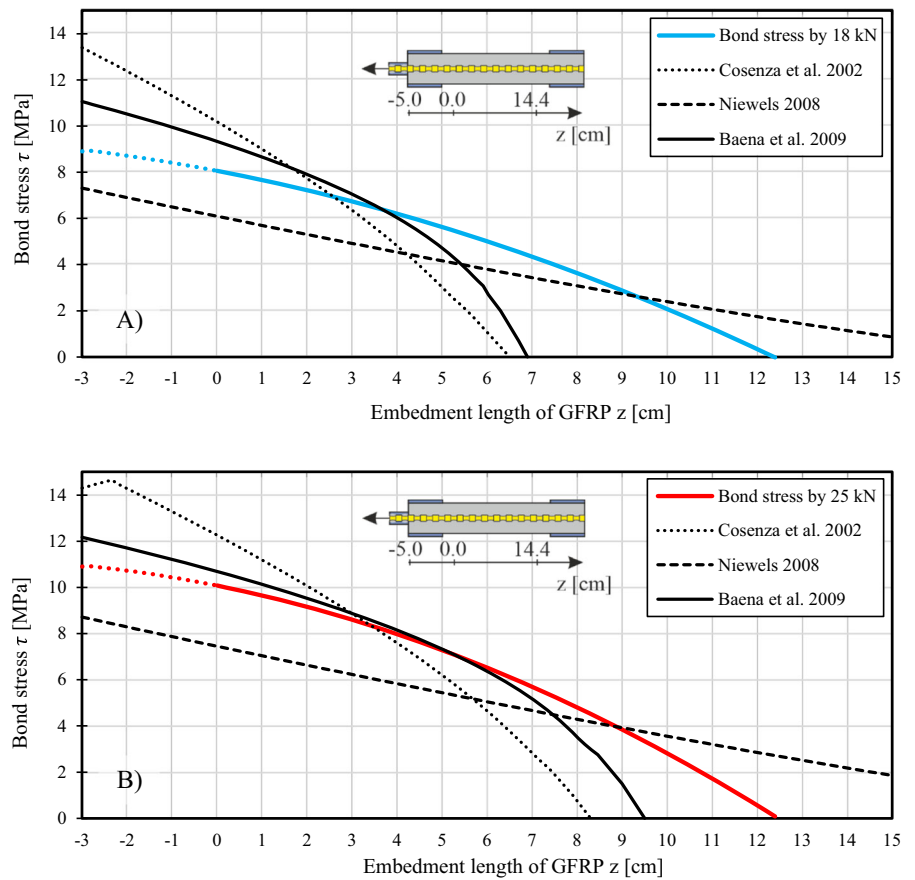
higher than in our tests. The solution may be Eq. (10) proposed by Caspari [21] taking into account the mean value of the compressive strength f_{cm} in the coefficient C:

$$C = 4.05 \cdot \sqrt{f_{cm}} \tag{10}$$

Baena et al. [20] did not propose a general bond-slip law, but used the approaches suggested in [18, 23, 63]. The model parameters for the ascending branch were reported and obtained in the experimental database including mean values. In the bond stress-slip relationship, Baena et al. used empirical coefficients s_m as divider. The coefficient s_m is the slip value at which the average bond strength is observed. Baena et al. [20] suggested for $\tau(s)$ Eq. (11):

$$\tau(s) = C \cdot \left(\frac{s(z)}{s_m} \right)^{\alpha} \tag{11}$$

Analysis results derived from this formula agree with the course derived from our experimental results (Fig. 10). The bond stress curves for the second load step (25 kN) in the experiment coincide well with the curve from the bond-slip law (Eq. 7). The remaining differences are due to calibrating $\tau(s)$ in the constitutive law based on the pull-out tests with the slip measured on the unloaded rebar side. In our test, the slip on the unloaded side of the rebar was not observed. Nevertheless, the model according to Baena et al. is suitable for calculating the bond stress-slip relation on the z-axis of the GFRP rebar with a diameter of 8 mm. This holds true for calculating the anchorage length of reinforcement in concrete, too.

5 Conclusions

We investigated how the concrete's microstructure affects the force redistribution in concrete and reallocation of stresses in a GFRP reinforcement. We showed that the geometry of GFRP rebars like surface profile influences the pore distribution in concrete samples. The pore volume change around the concreted reinforcement and the bond stresses of the GFRP rebar were found to correlate. The pore volume change corresponds to the increase of strain and slip and therefore to the increase of normal stress in the rebar.

Non-destructive 3D imaging by CT and subsequent quantitative image analysis were used to analyze the microstructure of the concrete with the GFRP rebar. Scrupulous image processing ensured fair comparability of CT images of the sample taken at the three considered stages of the pull-out test. This enabled detailed quantitative analysis of the concrete microstructure along the height of the cylindrical sample (z-direction).

The pore volume change descends with increasing depth in the sample, away from the top where the force was applied. At the bottom of the sample, no visible change around the rebar was observed.

The experimental results could be compared nn the basis of the bond-slip constitutive law. Bond behavior models from the literature were compared to our $\tau - s$ relationship derived from the measured volume change and found to agree only quantitatively in the upper part of the sample. Larger deviations were observed at the end of the sample. The experimental results stay nevertheless within the range of known models. The bond model of Baena et al. corresponds best with the bond-slip relationship found in our experimental test in the load phase 25 kN for both, the bond stress as well as the length of the anchorage of the rebar. However, further investigation is needed to verify the method proposed here for other types of reinforcement.

For thorough validation of the empirical findings presented here, a variety of GFRP rebars in concretes of varying strengths and mix design have to be investigated. In particular, the diameter, anchor length, and profile and type of the bar should be varied. It would be interesting to study GFRP rebars with respect to damage [2, 59], where the weakening of the bond connection is advanced. Moreover, shorter load stages should be studied, not necessarily with greater pull-out force. Furthermore, bi-directionally or multi-directionally loaded samples should be examined. However, the latter requires much more sophisticated experimental setups in order to maintain the load during CT scans without disturbing the imaging. This much more sophisticated experimental setup could also reveal the source of the observed negative pore volume changes.

References

1. Alexander M, Beushausen H (2019) Durability, service life prediction, and modelling for reinforced concrete structures – review and critique. Cem Concr Res 122:17–29. https://doi.org/10.1016/j.cemconres.2019.04.018

2. Cromwell JR, Harries KA, Shahrooz BM (2011) Environmental durability of externally bonded FRP materials intended for repair of concrete structures. Constr Build Mater 25:2528–2539. https://doi.org/10.1016/j.conbuildmat.2010.11.096

3. Ehsani MR, Saadatmanesh H, Tao S (1996) Design Recommendation for Bond of GFRP Rebars to Concrete. J Struct Eng 122(3):247–54. https://doi.org/10.1061/(ASCE)0733-9445(1996)122:3(247)

4. Focacci F, Nanni A, Bakis C (2000) Local bond-slip relationship for FRP reinforcement in concrete. J Comp Construct (4 (1)):24–31. https://doi.org/10.1061/(ASCE)1090-0268(2000)4:1(24)

5. Vemuganti S, Chennareddy R, Riad A, Taha M (2020) Pultruded GFRP reinforcing bars using nanomodified vinyl ester. Materials 13(24):5710. https://doi.org/10.3390/ma13245710

6. Lin X, Zhang YX (2013) Bond–slip behavior of FRP-reinforced concrete beams. Constr Build Mater 44:110–117. https://doi.org/10.1016/j.conbuildmat.2013.03.023

7. Kharal Z, Sheikh S (2017) Tension stiffening and cracking behavior of glass fiber reinforced polymer-reinforced concrete. ACI Struct J 114(2). https://doi.org/10.14359/51689420

8. Jabbar SA, Farid SB (2018) Replacement of steel rebars by GFRP rebars in the concrete structures. Karbala Int J Mod Sci 4:216–227. https://doi.org/10.1016/j.kijoms.2018.02.002

9. Basaran B (2021) Effect of steel–FRP ratio and FRP wrapping layers on tensile properties of glass FRP-wrapped ribbed steel reinforcing bars. Mater Struct 54(5):188. https://doi.org/10.1617/s11527-021-01775-x(0123456789(),-volV)(01234567

10. Leonhard F (1988) Cracks and crack control in concrete structures. PCI J 33(4):124–45. https://doi.org/10.15554/pcij.07011988.124.145

11. Beeby A (2004) The influence of the parameter ϕ/ρ_{eff} on crack widths. Struct Concrete 5(2):71–83

12. Zilch K, Zehetmaier G (2010) Bemessung im konstruktiven Betonbau: Nach DIN 1045–1 (Fassung 2008) und EN 1992–1–1 (Eurocode 2). 2nd ed. Springer, Berlin

13. Fingerloos F (2016) Eurocode 2 für Deutschland: DIN EN 1992–1–1 Bemessung und Konstruktion von Stahlbeton- und Spannbetontragwerken—Teil 1–1: Allgemeine Bemessungsregeln und Regeln für den Hochbau mit Nationalem Anhang Kommentierte Fassung. 2nd ed. Beuth Verlag GmbH; Wilhelm Ernst & Sohn Verlag für Architektur und technische, Berlin

14. Erläuterungen zu DIN EN (2020) 1992–1–1 und DIN EN 1992–1–1/NA—Buch mit E-Book. 2nd ed. Berlin: Beuth

15. Vilanova I, Baena M, Torres L, Barris C (2015) Experimental study of bond-slip of GFRP bars in concrete under sustained loads. Compos B Eng 74:42–52. https://doi.org/10.1016/j.compositesb.2015.01.006

16. Hofmann S, Krieger L, Bujotzek L (2023) Calibration of a bond law for sand-coated BFRP reinforcement. https://doi.org/10.21203/rs.3.rs-2704336/v1

17. Pecce M, Manfredi G, Realfonzo R, Cosenza E (2001) Experimental and analytical evaluation of bond properties of GFRP bars. J Mater Civ Eng 13(4):282–290. https://doi.org/10.1061/(ASCE)0899-1561(2001)13:4(282)

18. Cosenza E, Manfredi G, Realfonzo R (2002) Development length of FRP straight rebars. Compos B Eng 33(7):493–504. https://doi.org/10.1016/S1359-8368(02)00051-3

19. Niewels J (2008) Load carrying behavior of concrete members with fibre reinforced polymers. RWTH Aachen, Aachen, Germany

20. Baena M, Torres L, Turon A, Barris C (2009) Experimental study of bond behavior between concrete and FRP bars using a pull-out test. Compos B Eng 40(8):784–797. https://doi.org/10.1016/j.compositesb.2009.07.003

21. Caspari C.(2022) Zur Verbundverankerung von Glasfaserkunststoffbewehrungsstäben in Betonbauteilen unter Kurzzeit- und Langzeitbeanspruchung. Kaiserslautern, Germany: Doctoral dissertation, TU Kaiserslautern

22. Masmoudi R, Masmoudi A, Ouezdou MB, Daoud A (2011) Long-term bond performance of GFRP bars in concrete under temperature ranging from 20−80 °C. Constr Build Mater 25(2):486–493. https://doi.org/10.1016/j.conbuildmat.2009.12.040

23. Eligehausen R, Popov E, Bertero V (1983) Local bond stress–slip relationships of deformed bars under generalized excitations: Report no. 83/23 of the National Science Foundation. Berkeley

24. Yan F, Lin Z, Yang M (2016) Bond mechanism and bond strength of GFRP bars to concrete: a review. Compos B Eng 98:56–69. https://doi.org/10.1016/j.compositesb.2016.04.068

25. Alves J, El-Ragaby A, El-Salakawy E (2011) Durability of GFRP bars' bond to concrete under different loading and environmental conditions. J Compos Constr 3:249–262. https://doi.org/10.1061/(ASCE)CC.1943-5614.0000161

26. Achillides Z (1998) Bond behavior of FRP bars in concrete: The University of Sheffield

27. Alves J, El-Ragaby A, El-Salakawy E (2010) Bond strength of glass FRP bars in concrete subjected to freeze-thaw cycles and sustained loads. In: CICE 2010—The 5th international conference on FRP composites in civil engineering Beijing China

28. Rehm G (1961) The fundamentals of bond between steel reinforcement and concrete. Ernst & Sohn, Berlin, Germany

29. RILEM RC 6 (1994) Bond test for reinforcement steel: pull-out test, international union of testing and research laboratories for materials and structures

30. Gudonis E, Kačianauskas R, Weber A, Kaklauskas G (2014) Mechanical properties of the bond between GFRP reinforcing bars and concrete. Mech Compos Mater 4:457–466. https://doi.org/10.1007/s11029-014-9432-0

31. Füllsack-Köditz R (2004) Bond characteristics of GFRP-rebars and cracking formation of GFRP reinforced concrete structures. Doctoral dissertation, Bauhaus-Universität Weimar, Weimar

32. Clauß F, Ahrens MA, Mark P (2022) Thermo-mechanical experiments on reinforced concrete beams: assessing thermal, mechanical, and mixed impacts on fiber optic measurements. Struct Concrete. https://doi.org/10.1002/suco.202100890

33. Balázs G, Czoboly O, Lublóy É (2016) Computed tomography: new possibilities testing of concrete. fib Symposium. Performance-Based Approches for Concrete Structures. University of Cape Town

34. Balázs GL, Czoboly O, Lublóy É, Kapitány K, Barsi Á (2017) Observation of steel fibres in concrete with Computed tomography. Constr Build Mater 140:534–541. https://doi.org/10.1016/j.conbuildmat.2017.02.114

35. Schnell J, Schladitz K, Schuler F (2010) Direction analysis of fibres in concrete on basis of computed tomography. Beton- und Stahlbetonbau 105(2):72–77

36. Du Plessis A, Boshoff WP (2019) A review of X-ray computed tomography of concrete and asphalt construction materials. Constr Build Mater 199:637–651. https://doi.org/10.1016/j.conbuildmat.2018.12.049

37. Dybeł, P.; Kucharska, M (2021) X-ray CT Investigation of bond mechanism in reinforced SCC elements of different placement technology. Materials (Basel) 14. https://doi.org/10.3390/ma14216236.

38. Oesch T (2016) In-situ CT investigation of pull-out failure for reinforcing bars embedded in conventional and high-performance concretes. In: 6th Conference on industrial computed tomography, Wels, Austria 2016. e-Journal of Nondestructive Testing Vol. 21(2). https://www.ndt.net/?id=18788

39. Kronenberger M, Schladitz K, Hamann B, Hagen H (2018) Fiber segmentation in crack regions of steel fiber reinforced concrete using principal curvature. Image Anal Stereol 37:127–137

40. Dybeł P (2021) Effect of bottom-up placing of self-compacting concrete on microstructure of rebar-concrete interface. Constr Build Mater 299:124359. https://doi.org/10.1016/j.conbuildmat.2021.124359

41. Paetsch O, Baum D, Prohaska S, Ehrig K, Meinel D, Ebell G (2015) 3D corrosion detection in time-dependent CT images of concrete. In: Proceeding digital industrial radiology and computed tomography, Ghent, Belgium. J Nondestruct Test 20(8) . https://www.ndt.net/?id=18043

42. EN 12620 (2008) Aggregates for Concrete. Beuth Verlag GmbH, Berlin, Germany

43. Chen X, Wu S, Zhou J (2014) Experimental study and analytical model for pore structure of hydrated cement paste. Appl Clay Sci 101:159–167. https://doi.org/10.1016/j.clay.2014.07.031

44. EN 12390–2:2019 (2019) Testing hardened concrete—part 2: Making and curing specimens for strength tests. Beuth Verlag GmbH, Berlin, Germany

45. EN 12390–3:2019 (2019) Testing hardened concrete -Part 3: Compressive strength of test specimens. Beuth Verlag GmbH Berlin, Germany

46. Capozucca R, Ricci V (2016) Bond of GFRP strips on modern and historic brickwork masonry. Compos Struct 140:540–555. https://doi.org/10.1016/j.compstruct.2015.12.047

47. Schöck Bauteile GmbH (2015) Technical Information: Schöck Combar®, Baden, Germany

48. DIBt. Approval Z-1.6–238 (2018) Schöck ComBAR reinforcing bar made from glass fibre reinforced plastic. Berlin, Germany

49. Canadian Standards Association (2012) Design and construction of building structures with fibre-reinforced polymers(CSA S806–12). Ontario, Canada

50. Nguyen T, Ghazlan A, Kashani A, Bordas S, Ngo T (2018) 3D meso-scale modelling of foamed concrete based on X-ray Computed Tomography. Constr Build Mater 188:583–598. https://doi.org/10.1016/j.conbuildmat.2018.08.085

51. Maryamh K, Hauch K, Redenbach C, Schnell J (2021) Influence of production parameters on the fiber geometry and the mechanical behavior of ultra high performance fiber-reinforced concrete. Struct Concr 22(1):361–375. https://doi.org/10.1002/suco.202000105

52. Maryamh K, Hauch K, Redenbach C, Schnell J (2021) Influence of specimen size on the fibre geometry and tensile strength of ultra-high-performance fibre-reinforced concrete. Struct Concr. https://doi.org/10.1002/suco.202000753

53. Fraunhofer ITWM. MAVI—Modular algorithms for volume images: quantitative analysis of microstructures. Kaiserslautern, Germany.

54. Fraunhofer ITWM. ToolIP—Tool for Image Processing: User Manual. Kaiserslautern, Germany.

55. Ohser J, Schladitz K (2009) 3D Images of materials structures: processing and analysis. Wiley-VCH, Weinheim, Germany

56. Ametrano D (2011) Bond characteristics of glass fibre reinforced polymer bars embedded in high performance and

ultra-high performance concrete. Ryerson University, Toronto, Ontario, Canada

57. Hossain KMA (2018) Bond Strength of GFRP Bars Embedded in Engineered Cementitious Composite using RILEM Beam Testing. Int J Concr Struct Mater 12(1). https://doi.org/10.1186/s40069-018-0240-0

58. Puck A, Mannigel M (2007) Physically based non-linear stress–strain relations for the inter-fibre fracture analysis of FRP laminates. Compos Sci Technol 67(9):1955–1964. https://doi.org/10.1016/j.compscitech.2006.10.008

59. EN 12390–13 (2019) Testing hardened concrete—Part 13: Determination of secant modulus of elasticity in compression. Beuth Verlag GmbH, Berlin, Germany

60. The International Federation for Structural Concrete (fib) model code for concrete structures 2010. Ernst & Sohn, Berlin 2013

61. Małecki T, Marzec I, Bobiński J, Tejchman J (2007) Effect of a characteristic length on crack spacing in a reinforced concrete bar under tension. Mech Res Commun 34(5–6):460–465. https://doi.org/10.1016/j.mechrescom.2007.04.002

62. Niewels J, Hegger J (eds) (2010) Concrete members with Fibre Reinforced Polymers (FRP). Beuth Verlag GmbH

63. Cosenza E, Manfredi G, Realfonzo R (1995) Analytical modelling of bond between FRPreinforcing bars and concrete. Proceedings of secondinternational RILEM symposium (FRPRCS-2), pp 164–71